ARTICLE

Check for updates

Residual polymer stabiliser causes anisotropic electrical conductivity during inkjet printing of metal nanoparticles

Gustavo F. Trindade [1,2✉], Feiran Wang[2], Jisun Im [2], Yinfeng He[2], Adam Balogh[2], David Scurr [1], Ian Gilmore [3], Mariavitalia Tiddia[3], Ehab Saleh[2,4], David Pervan[2], Lyudmila Turyanska [2], Christopher J. Tuck[2], Ricky Wildman [2], Richard Hague[2] & Clive J. Roberts[1✉]

Inkjet printing of metal nanoparticles allows for design flexibility, rapid processing and enables the 3D printing of functional electronic devices through co-deposition of multiple materials. However, the performance of printed devices, especially their electrical conductivity, is lower than those made by traditional manufacturing methods and is not fully understood. Here, we reveal that anisotropic electrical conductivity of printed metal nanoparticles is caused by organic residuals from their inks. We employ a combination of electrical resistivity tests, morphological analysis and 3D nanoscale chemical analysis of printed devices using silver nanoparticles to show that the polymer stabiliser polyvinylpyrrolidone tends to concentrate between vertically stacked nanoparticle layers as well as at dielectric/ conductive interfaces. Understanding the behaviour of organic residues in printed nanoparticles reveals potential new strategies to improve nanomaterial ink formulations for functional printed electronics.

[1] Advanced Materials and Healthcare Technologies, School of Pharmacy, University of Nottingham, University Park, Nottingham, UK. [2] Centre for Additive Manufacturing, Faculty of Engineering, University of Nottingham, Jubilee Campus, Nottingham, UK. [3] National Physical Laboratory, Teddington, UK. [4] Future Manufacturing Processes Research Group, Faculty of Engineering and Physical Sciences, University of Leeds, Leeds, UK. ✉email: Gustavo.FerrazTrindade@nottingham.ac.uk; Clive.Roberts@nottingham.ac.uk

Digitally printed electronics are a driver for novel research in various fields owing to their design flexibility as well as other advantages such as expedited time-to-market[1–3]. Ink jetting of inks containing colloidal materials, such as metal nanoparticles[4–8], germania-silica[9], semiconductor quantum dots[10], intrinsically conductive polymer colloids[11] and magnetic nanoparticles[12], have been successfully employed in applications ranging from flexible and wearable electronics[2,7,13–19] to quantum optoelectronic devices[20–22] and fully printed perovskite solar cells[23–26]. However, the performance of printed parts is not competitive with those made by traditional manufacturing methods. This is due to challenges in both manufacturing techniques and choices of materials, of which there is a lack of comprehensive understanding. Metal nanoparticles are among the most commonly used conductive materials for printed electronics, and typically require consolidation via a two-step process: solvent evaporation upon printing (pinning) and subsequent low-temperature sintering (120–200 °C)[4,15,27–30], enabling conductive tracks on polymer substrates[2,4,7]. More recently, inkjet-based three-dimensional (3D) printing has been used to enable the selective co-deposition of different functional materials contemporaneously (i.e. dielectric and/or conductive materials)[4,5,14,27,31,32] to ultimately achieve the production of macroscopic multi-material objects with multiple functionalities.

Despite significant interest in utilising metal nanoparticle-based materials in two-dimensional (2D) and 3D printed electronic devices, the lower and anisotropic intra-layer (planar) and inter-layer (vertical) conductivity of metal nanoparticle layers, compared to bulk metals, limits device performance and hence uptake in industry and products[4]. The conductivity of printed layers are known to be dependent on thermal treatment profiles and have been previously attributed to morphological changes and possible organic residues[4,30,33,34]. However, the detailed mechanism of low-temperature sintering of metal nanoparticles that leads to reduced conductivity remains to be fully understood.

Organic molecules are used in inks as stabilisers or capping agents to enable nanoparticle dispersion in low-viscosity solvents; however, their residues are likely to hinder device performance[33], even when present in very small amounts. Surface sensitive chemical analysis techniques of time-of-flight secondary ion mass spectrometry (ToF-SIMS) and X-ray photoelectron spectroscopy (XPS), in combination with gas cluster ion beams (GCIBs), are a powerful toolset for depth profiling organic materials with high chemical specificity, sensitivity, and nanometre depth resolution[35–43], chemical imaging of buried hybrid organic/inorganic interfaces[44,45] and characterisation of core–shell structures[46–52].

Here, we present a comprehensive study of the effect of residues of an organic stabiliser in inkjet-printed silver nanoparticles (AgNPs). We show that residues tend to concentrate between vertically stacked layers, which correlates with reduced and anisotropic electrical conductivity before and after low-temperature sintering. Our results provide new insights on routes to improve intra-layer AgNPs sintering and overcome functional anisotropy and hence improve uptake of this potential transformational technology. Our methodology is transferable to other nanomaterial-based inks and relevant for the development and exploitation of both 2D and 3D printed electronics.

Results
Distribution of polymer stabiliser upon printing of AgNPs. To investigate the interface of AgNPs during the inkjet printing and pinning process, we carried out high specificity chemical analysis of samples under a selection of printing conditions. As a result, we have found polyvinylpyrrolidone (PVP) on the surface of

printed layers of AgNPs by means of the unambiguous identification of characteristic PVP signal[36,53] using a novel 3D orbi-SIMS instrument[54] and XPS (Fig. 1 and Supplementary Fig. 1). PVP is a commonly used stabiliser, reducing agent, and shape-controlling agent for the synthesis of metal nanoparticles[55,56]. As a capping agent, it makes AgNPs disperse well in aqueous and organic solvents due to its amphiphilic characteristics derived from the highly polar amide group within the pyrrolidone ring and hydrophobicity from the methylene backbone. PVP thus plays a vital role in dispersing and stabilising AgNPs in solvents for stable ink formulation[56]. However, PVP does not completely decompose under typical multi-material jetting and sintering temperatures (up to 150 °C)[5] and its residues are likely to remain. Understanding the state and distribution of PVP upon inkjet printing and post-deposition treatment of AgNPs is essential to develop solutions that minimise its impact on the performance of printed electronics.

Inkjet printing of AgNPs starts with printing and then pinning the material by removing the solvent (Fig. 1a). All printing was conducted on a hot stage at $T = 90$ °C, which is sufficient for pinning the printed ink with minimal AgNPs sintering. This temperature is also low enough to prevent printhead damage and polymeric substrate degradation. The chemical mapping data from the top surface of a printed layer of AgNPs (Fig. 1b) and individually deposited droplets (Fig. 1c, d) show a "coffee ring" effect where the solute (PVP) and suspending nanoparticles tend to flow towards its pinned contact line following the outward flow initiated by the combination of evaporation and contact-line pinning effect[57,58]. This is observed as a pattern with PVP-rich lines at the edge of each swath of ink across the entire surface (Fig. 1b)[57,59]. The presence of PVP, even if at very low concentrations, can hinder the sintering of nanoparticles at the interface, leading to reduced conductivity in the inter-layer (vertical) direction[4]. In a 3D printing context, subsequently deposited AgNPs layers will therefore encounter a PVP-rich surface and these organic molecules may become trapped at the interface. We examined the 3D distribution of PVP, via ToF-SIMS depth profiling, within a sample consisting of four successively printed layers of AgNPs ink. The results (Fig. 2a, b) show that the top surface has the strongest PVP signal intensity, and that PVP signal was also detected through the bulk. Moreover, the PVP intensity oscillates with an average period of 282.8 nm and peaks at approximately 300, 600 and 900 nm depth, as confirmed by fast Fourier transform analysis (Supplementary Fig. 5a). These peaks, based on the single-layer data (Supplementary Fig. 2) and recent related work[60], are observed at the depths corresponding to the position of interfaces between individual printed layers. This is consistent with our hypothesis that PVP concentrates at the interface between printed layers (Fig. 2d) and suggests that this happens during the layer-wise printing process.

To confirm that the observations of organic residues in ToF-SIMS for our AgNP samples is not related to measurement artefacts reported previously in more complex samples, such as perovskite solar cells[61,62], we carried out XPS measurements. The high-resolution XPS N1s spectrum recorded for the printed AgNPs sample (Fig. 2c) revealed that the non-interacting form of PVP, represented by C–N at 400 eV, is more abundant at the top surface, while the interacting form represented by C–N–Ag at 398 eV has a stronger signal in the bulk (~100 nm deep)[63]. We deduce that the non-interacting form of PVP is that of unbound PVP residues in the ink. This, in conjunction with the ToF-SIMS depth profile (Fig. 2b), indicates that non or weakly interacting PVP tends to migrate to the outer surface of the ink, forming a thin coating on the top surface upon solvent evaporation (Fig. 2d). However, non or weakly interacting PVP was also detected in
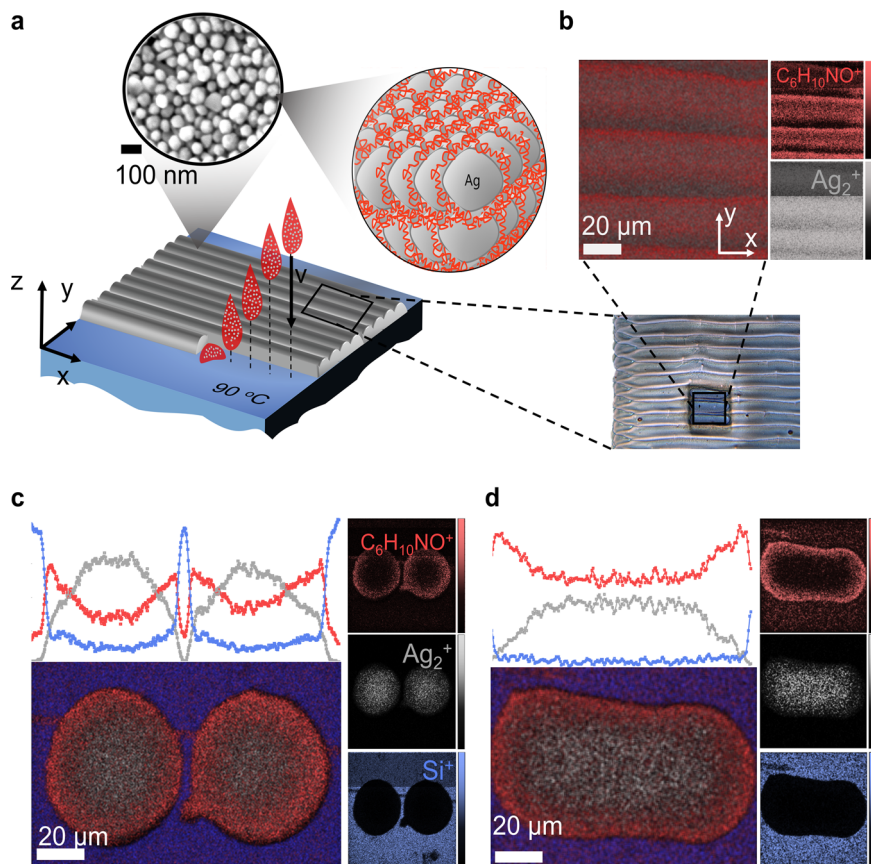
Fig. 1 inkjet printing AgNPs and detection of polymer stabiliser. a Drop-on-demand jetting of inks containing AgNPs with in situ solvent evaporation (pinning). The AgNPs size distribution of the ink is detailed in Supplementary Fig. 3. **b** Optical image (bottom) of a printed layer of AgNPs and chemical maps (top) showing the distribution of Ag_2^+ (grey), $C_6H_{10}NO^+$ (red), and Si^+ (blue) at the surface of a printed layer, **c** pair of deposited droplets and **d** two coalesced droplets. The line plots represent the intensity across the centre of each map.

between-printed layers with relatively high intensity. In order to obtain enhanced depth resolution of chemical information within the printed material, we carried out ToF-SIMS depth profiling using a lower energy and lower current for the etching ion beam (Fig. 3) (details in "Methods"). Principal component analysis (PCA) using depth levels as observations and a list of peaks as variables (Fig. 3b, c PC 2 with 20.43% of total variance—full PCA results are shown in Supplementary Fig. 4) revealed a secondary, more complex, oscillating pattern within a single printed layer with an average period of 80.7 nm (confirmed by fast Fourier transforms in Supplementary Fig. 5b), which is compatible with the average diameter of individual AgNPs in the ink (60 ± 22 nm, Supplementary Fig. 3). The slightly higher length is attributed to nanoparticles packing and the oscillating pattern alternates between characteristic ions for silver (such as Ag^+, $^{109}Ag^+$ and Ag_2^+) and PVP (such as $C_4H_6NO^+$ and $C_6H_{10}NO^+$). We interpret that this is related to the core–shell structure of AgNPs/PVP with the irregularities in the signal arising from differences in sputter rates and the average PVP distribution on the surface of several Ag nanoparticles within the ToF-SIMS analysis area.

In this nanoparticle-resolution depth profile, we tracked the signal of more specific secondary ions related to the cyclic amide of pyrrolidone ($C_6H_{10}NO^+$), linear hydrocarbon ($C_4H_7^+$), the cyclic amide-silver ($C_4H_6NOAg^+$) and silver (Ag^+) and normalised their signals by their maximum intensity (Fig. 3d, e). We observed that each ion signal peaks at different depths, revealing molecular-level information. These results give evidence of the interaction of PVP with the AgNPs surface (Fig. 3a), in agreement with what has been previously predicted via molecular dynamics

simulations[64–67]. Every data point in the ToF-SIMS depth profile represents only the first few nanometres of that depth level; moreover, none of the secondary ion intensities decrease to zero within an oscillation, which is related to the fact that the capping polymer is present on the surface of all AgNPs.

Influence of sintering temperature on the distribution of residual polymer stabiliser and electrical resistivity. Sintering is a commonly used post process to promote inter-particulate bridging as well as the removal of residual organics. To evaluate how this process affects chemical, morphological and electrical properties of printed samples, the AgNPs were deposited and pinned as both single-layer and 200-layer electrodes and post-processed in an argon-filled oven at different temperatures (T) up to 500 °C. The resistivity of all samples was measured at room temperature (Fig. 4a, b, d), while their morphology was assessed by electron microscopy (Fig. 4c and Supplementary Fig. 6). The planar resistivity (ρ_{xy}) of the sample with a single printed layer decreased dramatically after processing at 100 °C and the resistivity remains ~13 μΩ cm for the samples sintered at the temperatures ranging from 100 to 200 °C. Micrographs of AgNPs show that the particles start bridging around these temperatures (Fig. 4c.ii–iv), hence forming conductive channels and leading to resistivity reduction. We noticed that ρ_{xy} of the AgNP samples with one printed layer remains about one order of magnitude higher than expected for bulk silver (black dashed line in Fig. 4d). A further increase of processing temperature to $T > 300$ °C results in an unexpected increase of ρ_{xy} for the single-layered samples due to inter-particle voids with diameters between 200 nm and
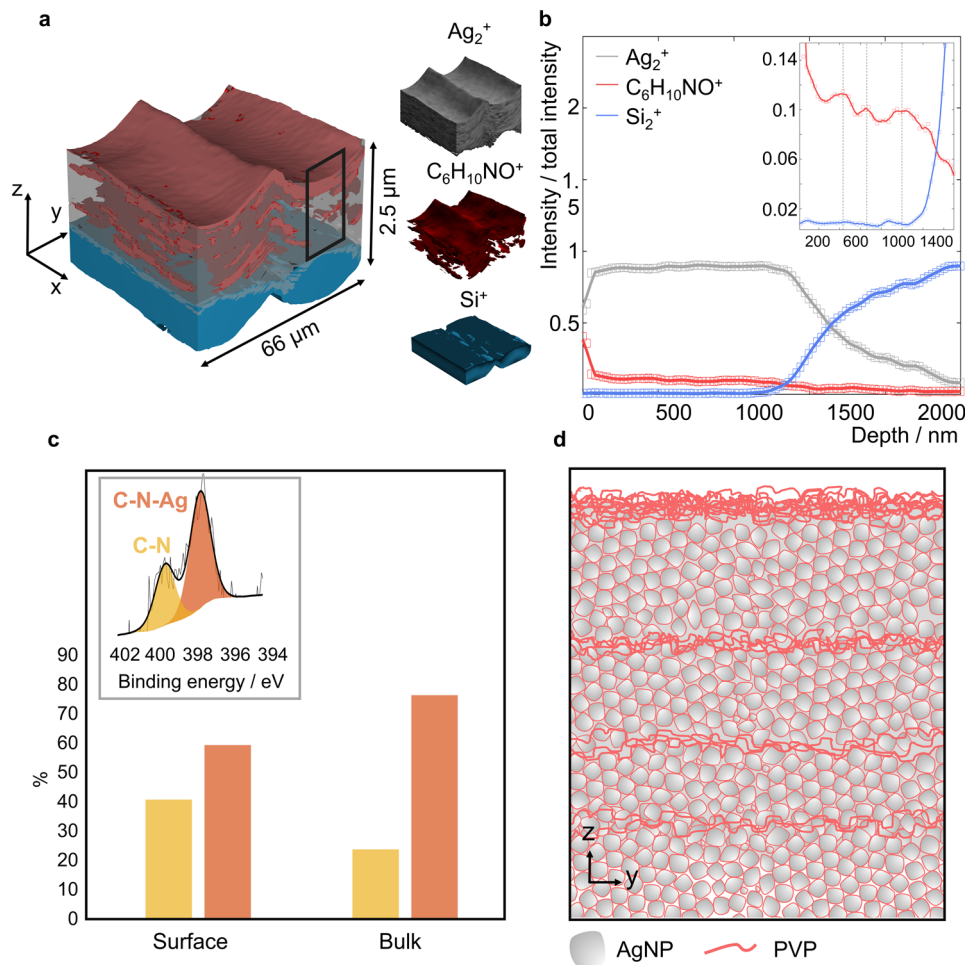
Fig. 2 3D chemical analysis of four stacked layers of inkjet 3D printed AgNPs. a 3D rendering of ToF-SIMS signal for Ag_2^+, $C_6H_{10}NO^+$ and Si^+. **b** Depth profile (averaged over an area of $50 \times 50\ \mu m^2$ per depth level) showing accumulation of PVP at layers interface. **c** XPS N1s data for non-interacting, free (C–N, 400 eV) and interacting (C–N–Ag, 398 eV) PVP with the Ag surface on top surface and bulk (~100 nm deep). **d** Illustration of cross-section of stacked AgNPs layers with PVP-rich interfaces.

500 nm shown in Fig. 4c.v. When the AgNPs were processed at 500 °C, the AgNPs agglomerated into macrostructures sized 1–5 μm with very poor continuity (Fig. 4c.vi). Those temperature ranges are specific for a silicon wafer substrate and may vary for a different substrate, depending on properties such as surface tension between ink and substrate. However, we propose that similar trends would be observed with continuity of conductive patterns being reduced once there is a predominance of melting over bridging. For multi-layer samples (200 layers), the planar resistivity, representing the intra-layer resistance, was in the range of 10 μΩ cm for all samples treated at T ~500 °C. This is due to the stacking of layers that filled the voids. However, the vertical resistivity (ρ_z), which was measured between top and bottom contacts in the perpendicular direction for the samples treated at $T = 130$ °C, is three orders of magnitude higher compared to planar resistivity, and independent of the number of printed layers. We measured $\rho_z = 23.6 \pm 8.4$ mΩ cm and $\rho_z = 23.5 \pm 9.4$ mΩ cm for the samples with 200 and 100 printed layers, respectively. These results, showing anisotropic resistivity, are consistent with the results of morphological studies. We employed XPS and ToF-SIMS to detect residual PVP at the surface of printed AgNPs after processing (Fig. 4e–h). The results show that PVP is still present after sintering the printed samples at temperatures between 100 and 230 °C, where resistivity is heavily anisotropic. Moreover, the proportion of non-interacting PVP (normalised ratio between XPS N1s peaks at 400 and 398 eV,

Fig. 4e) increases with processing temperatures at the top surface but decreases in the bulk (~100 nm deep). This confirms the hypothesis that weakly interacting PVP migrates to the surface (or layer interface in multi-layer samples) during sintering. These results also agree with thermal gravimetric analysis results that show a 70% weight loss between the temperatures of 150 and 250 °C, from solvent evaporation (Supplementary Fig. 7).

Residual PVP in a multi-material 3D printed conductive pattern. We applied the same methodology to map residual PVP within a fully 3D printed encapsulated conductive silver pattern that was produced via multi-material inkjet printing (Fig. 5a, b). The conductive channel consists of five printed layers of AgNPs processed using UV light and the dielectric material is tri(propylene glycol)diacrylate (TPGDA), represented by the secondary ion $C_3H_3O^+$. Details about the device and printing method are reported in our previous work[4,44]. As both the dielectric and conductive layers are printed contemporaneously, temperatures for in situ or post-processing must remain low to avoid damaging the organic material. Moreover, the glass transition temperature (T_g) of PVP is in the range 100–150 °C, depending on its molecular weight[56,68,69], which may lead to migration of PVP within the surface and interface of AgNPs during the post-processing sintering[66]. Chemical depth profiling results (Fig. 5c, e) show that residual PVP is present at higher quantities at the dielectric/conductive materials
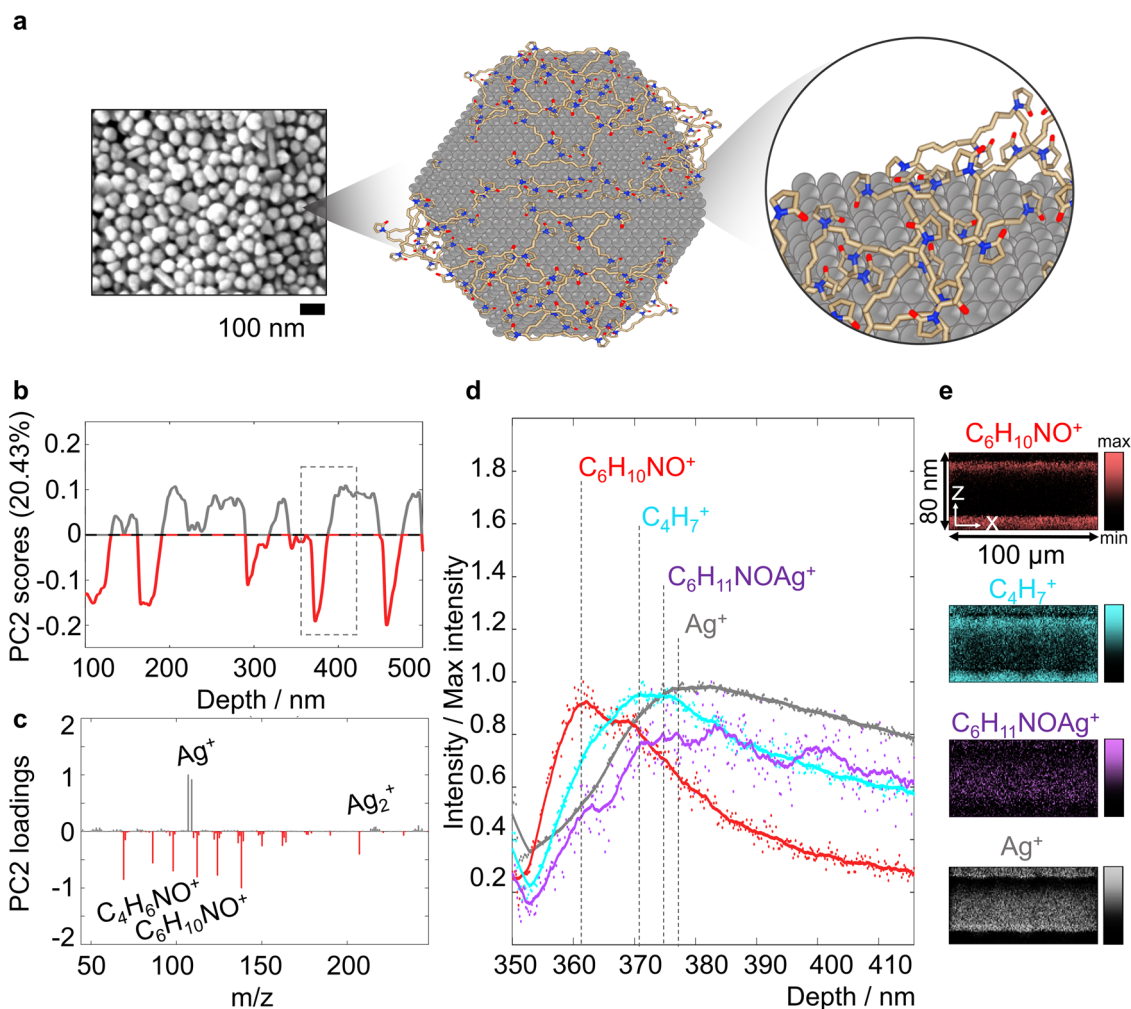
Fig. 3 PVP coordination onto AgNPs surface. a SEM micrograph of printed AgNPs and schematic showing PVP coordination on a single AgNP surface. **b** PCA scores and **c** loadings of depth profiling data at nanoparticle depth resolution. The dashed rectangle represents **d** depth profile within 100 nm showing signals for secondary ions $C_6H_{10}NO^+$, $C_4H_7^+$, $C_6H_{11}NOAg^+$ and Ag^+. **e** XZ maps within a depth of 80 nm. The data are averaged over an area of $100 \times 100~\mu m^2$ per depth level.

interface, in agreement with the results shown in Fig. 2, where greater signal of PVP was detected at the top surface of AgNPs printed layers. Furthermore, at the top TPGDA/AgNPs interface (Fig. 5c), silver is detected earlier in the depth profile than PVP. This is explained by transmission electron microscopy (TEM) micrographs of a cross-section of the device (Fig. 5d), which show interpenetration of AgNPs into the dielectric material. This is not observed at the bottom interface (Fig. 5e) because of the order in which materials are deposited: AgNPs deposited on a solidified layer of organic material have less mobility than when a liquid organic material is deposited onto a layer of AgNPs. A high level of interpenetration may affect cohesion between nanoparticles and consequently electrical conductivity. Investigations of the interfaces with high specificity are of great value in complex cases, such as inkjet-printed optoelectronic devices, and could provide valuable insights into the device operation. Control of the interface chemistry and morphology is essential to achieve the desired performance as it defines charge transfer processes, as was recently demonstrated also for inkjet-printed graphene transistor with AgNP top electrodes[60].

Discussion

We showed that poor inter- and intra-layer electrical conductivity in silver structures produced via 3D inkjet printing of AgNPs results

from a combined chemistry and morphology interface evolution during the low-temperature sintering process. This has been achieved via the determination of the 3D spatial distribution of residual polymeric capping agents within multiple printed layers. The residual polymer leads to anisotropic conductivity reduction as we showed that such organic residues accumulate at the interface of vertically stacked printed layers. With a clearer understanding of the distribution of residual organic stabiliser within the printed layers, it is possible to consider optimisation strategies to overcome the functional anisotropy of inkjet-based 3D printed electronics. When printing multiple layers, it is not practical to remove the part from the printer after each layer, especially when multiple materials are deposited contemporaneously (Fig. 5). In that case, post-processing strategies should be converted into in situ processing steps. When working with commercially available nanoparticulate ink formulations, the presence of a polymer stabiliser such as PVP is often inevitable, which therefore requires additional post-processing methods to overcome functional anisotropy. We showed that higher sintering temperatures are not always beneficial, not only because of potential damage to the substrate or contemporaneously deposited materials, but also because AgNPs tend to coalesce, resulting in further planar conductivity reduction. AgNPs have been proven to be sintered with ultraviolet (UV) and infrared (IR) light, which makes it the most likely processing route for printing 3D
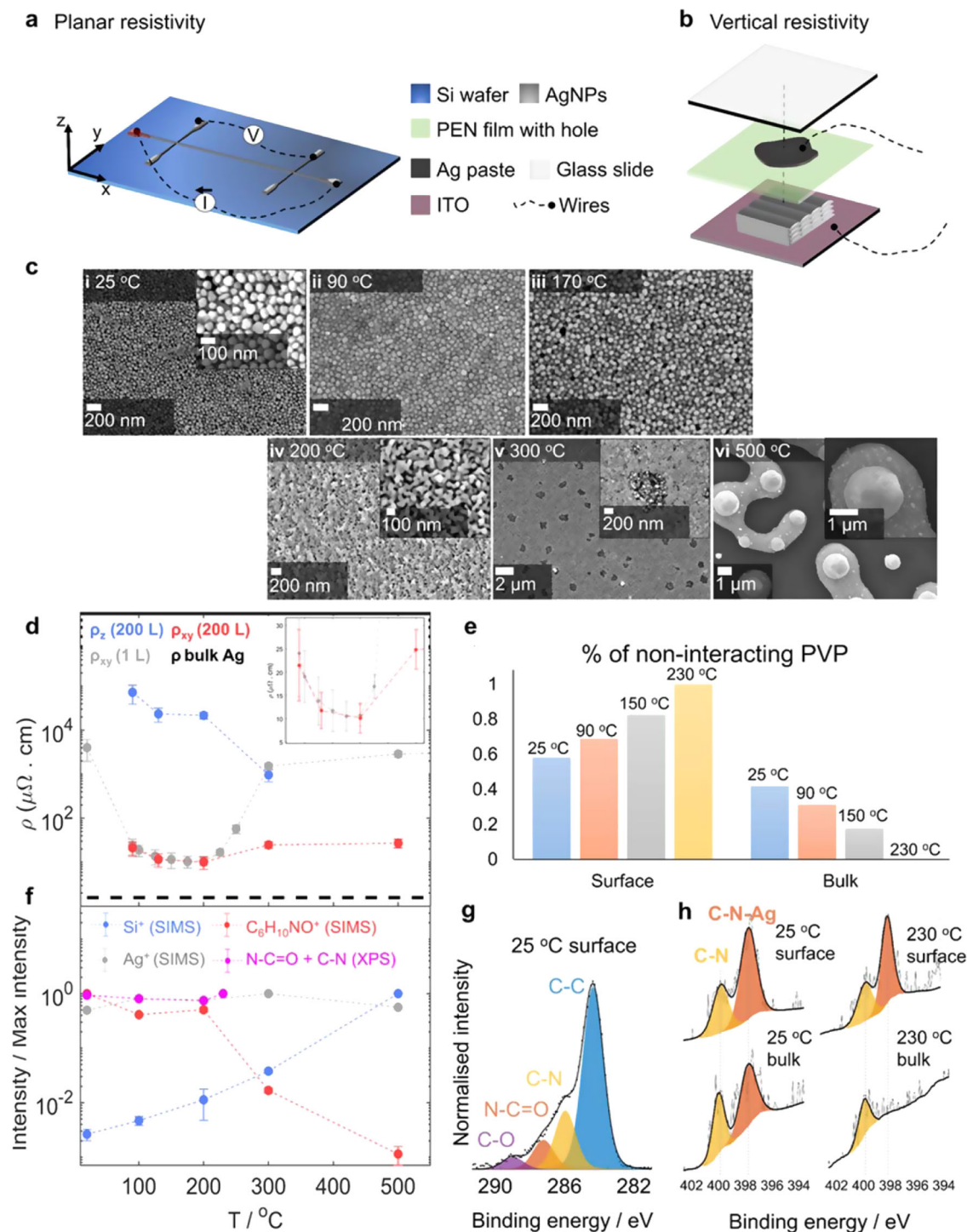
Fig. 4 Surface analysis, resistivity, and morphology of AgNPs printed and sintered at different temperatures. Schematic of **a** single layer and **b** multi-layer inkjet-printed AgNPs electrodes for planar and vertical resistivity measurements. **c** Secondary electron micrographs of AgNP samples sintered at different temperatures: (i) 25 °C, (ii) 90 °C, (iii) 170 °C, (iv) 200 °C, (v) 300 °C, (vi) 500 °C. **d** Dependence of planar (ρ_{xy}) and vertical (ρ_z) resistivity on sintering temperature for for single-layer and 200-layer samples. **e** Fraction of non-interacting PVP at the sample surface and bulk estimated from the XPS measurements for samples treated at different temperatures. **f** Normalised intensity of characteristic ToF-SIMS secondary ions for PVP ($C_6H_{10}NO^+$), silver (Ag^+) and the substrate (Si^+) and XPS C_{1s} peak-fitted[53] components $N-C=O+C-N$ as a function of sintering temperature. **g** XPS C1s and **h** N1s peak fitting for samples sintered at 25 and 230 °C. Details of the XPS peak-fitting parameters can be found in Supplementary Tables 1 and 2.

macrostructures[4,30]; therefore, the understanding of how a stabiliser behaves upon printing and sintering of metal nanoparticles is essential to aid ink formulation routes with different stabilisers that can either be removed at lower temperatures or be breakable upon excitation using UV or IR sources[70].

Methods

AgNPs ink used in this work was purchased from Advanced Nano Products (SilverJet DGP-40LT-15C) and was used as-received. The nominal composition of the ink consists of 38.85 wt% of AgNPs dispersed in triethylene glycol monomethyl ether and other additives. Thermogravimetry analysis and differential scanning calorimetry of silver NP inks were performed simultaneously on a TA Q600 unit.
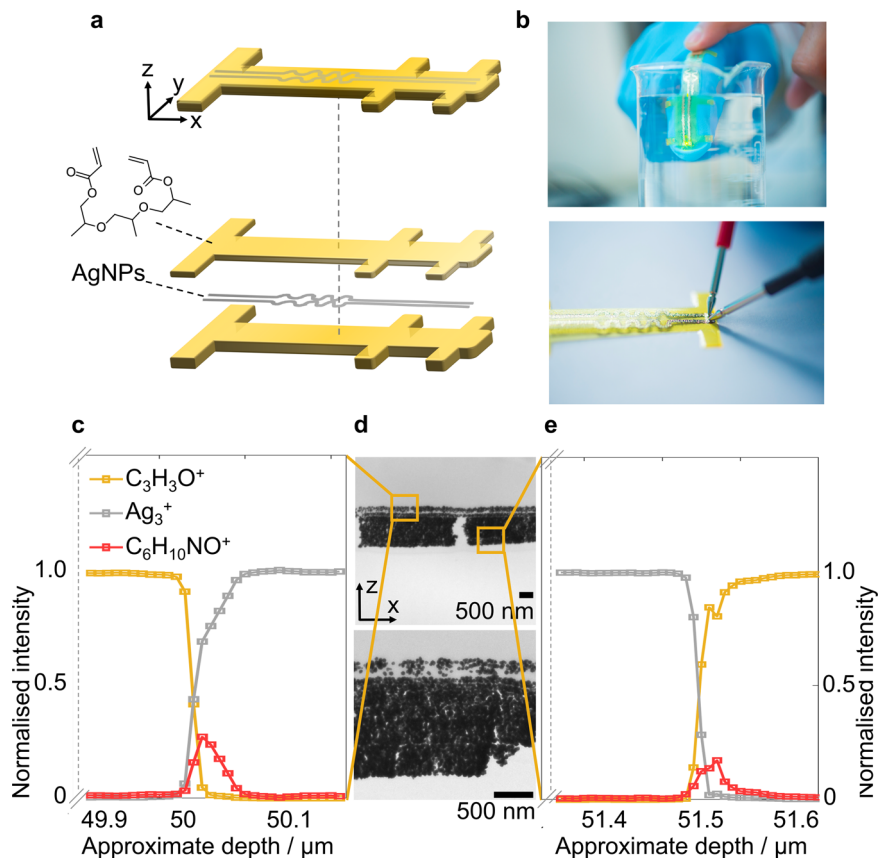
Fig. 5 Presence of residual stabiliser in a multi-material inkjet 3D printed encapsulated conductive silver pattern. a Schematic showing the layer structure of the device. **b** Photographs showing that encapsulation enables the use of the device under water. ToF-SIMS depth profile results at the **c** top and **e** bottom interface. The dielectric material is TPGDA and represented by $C_3H_3O^+$. PVP is represented by $C_6H_{10}NO^+$ **d** TEM micrographs of a cross-section.

The sample ink was placed and dried in a vacuum oven at 40 °C prior to the measurement. The sample was heated up at a temperature ramp of 10 °C min^{-1} under constant nitrogen flow of 100 ml min^{-1}.

AgNPs samples were printed using a Fujifilm Dimatix Materials Printer DMP-2850 Series with a 10 pL cartridge. The droplet diameter is ~45 µm and a drop spacing distance of 30 µm was used to ensure deposition of continuous layers and pattern uniformity. Only one nozzle was employed to maximise the morphological homogeneity and geometrical precision of deposition. The samples were printed on a Si/SiO$_2$ substrate. For all samples (apart of room temperature sample) the substrate was heated to 90 °C by an in situ resistance heater.

The encapsulated conductive pattern was inkjet 3D printed with co-deposition of the AgNPs and an organic ink made in-house and based on TPGDA. Both polymer and silver layers were printed and cured/sintered contemporaneously by a LED-based UV source connected to the print-heads of a PixDro LP50 printer. This sample was used to benchmark a sample preparation methodology previously published[44]. More details of the ink formulations and printing method are described elsewhere[4].

The planar resistivity of printed AgNPs samples was measured using a Keithley 2400 sourcemeter and a Keithley 7500 multimeter with a four-probe method, also known as the Kelvin technique, to eliminate contact resistance. A voltage is applied from the two probes at the ends and the current through the printed line was measured with the change of voltage drop across the two probes in the middle. Each I–V curve was measured three times using both forward and backwards scanning. The derivative of the I–V curve reveals the conductivity of the printed line with the precise geometry measured by an optical microscope. All measurements were repeated three times for at least three different samples, and results are presented as an average value with its standard deviation.

The vertical resistivity (ρ_z) of multiple printed layers of AgNPs was measured by printing 200 layers of the AgNP ink on ITO glass at 90 °C for good drying and pinning and sintering at 130, 200 and 300 °C. The morphology of the printed AgNP line on ITO substrate is comparable to that on Si/SiO$_2$ substrate, indicating that the ITO is suitable as a bottom contact for anisotropic resistivity comparison. A 75-µm-thick PEN film with a window of the same size and shape of the sample was put on top to expose the top layers and insulate the bottom contacts from the top contact. A glass slide with a wire and dried silver paste facing downwards are then pushed firmly on top of the sample and the PEN film as the top contact. The I–V curve is then measured using a Keithly sourcemeter to extract the resistance.

From all measurements, we could still observe a contact resistance for all samples. To work out the contact resistance, the same procedures have been repeated for 50 printed layers. The sample thicknesses were measured by scannning electron microscopy (SEM) cross-sections. By subtracting the resistance of thinner samples, the ρ_z values of different sintering temperatures can be obtained. Each measurement has been repeated three times for three different samples.

SEM was carried out using a JEOL 7100 F FEG-SEM instrument which uses an in-lens Schottky field emission source. The microscope was operated with a 5 keV electron beam and at a working distance of 5 mm. Samples were mounted on an aluminium stub using double-sided conductive carbon tape. Image analysis was done with ImageJ 1.49k.

TEM was carried out using a JEOL 2000 FX TEM with a 200 kV electron beam. Thin cross-sections of the encapsulated conductive pattern were prepared using a diamond knife in an Ultramicrotome PowerTome (RMC Products). Samples were embedded in epoxy resin before cutting.

XPS was carried out using an AXIS ULTRA instrument (Kratos) with a monochromated Al Kα X-ray source (1486.6 eV) operated at 10 mA emission current and 12 kV anode potential (120 W). Spectra were acquired with the Kratos VISION II software. A charge neutraliser filament was used to prevent surface charging. High-resolution spectra at pass energy 20 eV, a step of 0.1 eV, and sweep times of 10 min each were also acquired for photoelectron peaks from the detected elements and these were used to model the chemical composition. All spectra were charge corrected to the C 1s peak (adventitious carbon/CH$_2$) set to 284.8 eV. Peak fitting of the C1s and N1s scans was performed on the Casa XPS software (www.casaxps.com) using mixed Gaussian/Lorenzian components. Details of the fitting parameters are shown in Supplementary Tables 1 and 2.

Surface ToF-SIMS of AgNPs samples treated at different temperatures was carried out using a ToF-SIMS IV instrument (IONTOF GmbH). Secondary ion mass spectra were acquired in positive ion polarity mode using a 25 keV Bi$_3{}^+$ primary ion beam delivering 0.3 pA. The primary ion beam was raster scanned over different areas with the total ion dose kept under the static limit of 10^{13} ions/cm^2. The ToF analyser was set with 200 µs cycle time, resulting in a mass range between 0 and 3492 mass units and a low-energy (20 eV) electron flood gun employed to neutralise charge build up.

ToF-SIMS 3D mapping of AgNPs was carried out using a 3D OrbiSIMS (Hybrid SIMS) instrument from IONTOF GmbH. The ToF-SIMS data were acquired in positive ion polarity mode in dual-beam mode by raster scanning a 30 keV Bi$_3{}^+$

primary ion beam (delivering 0.08 pA) of 100×100 μm^2 at the centre of a 300×300 μm^2 sputter crater formed using an argon GCIB. The GCIB was operated in two conditions, high-energy with 20 keV and 2000 atoms in the cluster with 5 nA beam current and low energy using 10 keV and 1500 atoms per cluster delivering 3 nA. The analysis was performed in the "non-interlaced" mode with a low-energy (20 eV) electron flood gun employed to neutralise charge build up. For the low-energy settings, three sputter frames were performed per cycle with 15 analysis scans per cycle and a pause time in between cycles of 0.5 s. For the high-energy settings, five sputter frames were performed per cycle with 20 analysis scans per cycle and a pause time in between cycles of 0.5 s. The ToF analyser was set with 200 μs cycle time, resulting in a mass range between 0 and 2233 mass units.

ToF-SIMS depth profiling of multi-material device was carried out using a ToF-SIMS IV (IONTOF GmbH) in dual-beam mode by raster scanning a 25 keV Bi$_3^+$ primary ion beam (delivering 0.08 pA) of 100×100 μm^2 at the centre of a 300×300 μm^2 sputter crater formed using a 20 keV argon GCIB delivering 20 nA. The analysis was performed in the "non-interlaced" mode with a low-energy (20 eV) electron flood gun employed to neutralise charge build up. Five sputter frames were performed per cycle with 20 analysis scans per cycle and a pause time in between cycles of 0.5 s. The ToF analyser was set with 200 μs cycle time, resulting in a mass range between 0 and 2233 mass units. AgNPs/TPGDA interfaces were reached profiling from top and bottom surfaces. To reach the buried interfaces, the etching beam current had to be greater and acquisition time per level lower, which resulted respectively in limited depth resolution and lower signal-to-noise ratio to be able to detect PVP within layers of AgNPs in a similar manner to what is presented in Figs. 1 and 2.

ToF-SIMS data processing All ToF-SIMS intensity maps were normalised by total ion counts to correct for topographic features. All intensity maps were produced using the simsMVA software[71]. For 3D renders, voxel intensities were normalised by total ion counts to account for topographic features and the z-scale was corrected based on the substrate signal. The final 3D representations were created by combining rendered isosurfaces ranging from 30 to 50% of the maximum intensity for each ion. Multivariate analysis was carried out using the mass as the variables and each mass spectrum in the depth profile as the observations. For each depth profiling dataset, Surface Lab 7.1 (IONTOF GmbH) was used to perform an automated peak search on the total spectra restricted only to peaks with intensity higher than 100 counts and masses between 30 and 300 u. Dead-time corrected peak areas were then exported for each sequential mass spectrum in the depth profile. PCA was performed using the simsMVA software[71], which yields components loadings with groups of peaks that shared the same depth profile (scores). Prior to PCA, data was Poisson scaled to account for heteroscedasticity[72].

Orbitrap secondary ion mass spectrometry (OrbiSIMS) was carried out using a 3D OrbiSIMS (Hybrid SIMS) instrument[54]. A 20 keV Ar$_{3000}^+$ GCIB of 20 μm diameter, delivering 3.5 nA (with duty cycle set to 70.4%) was used as the primary ion beam. Depth profiling data were acquired over areas of 300×300 μm^2 using random raster mode with crater size 382×382 μm^2. The sample voltage was set at +57.5 V. Argon gas flooding was used to aid charge compensation and the pressure in the main chamber was maintained at 9.0×10^{-7} bar. The spectra were collected in positive polarity, in mass range 50–750 m/z. Mass resolving power was 218,726 at 200 m/z.

Optical profilometry was used to determine the crater depth after ToF-SIMS depth profiling experiments and calibrate the depth scale. Scans were obtained using a Zeta-20 optical microscope (Zeta Instruments) in a Z range of 4.6 μm. The number of steps was set to 328, allowing for a z step size of 14 nm.

Data availability

References

1. Kamyshny, A. & Magdassi, S. Conductive nanomaterials for 2D and 3D printed flexible electronics. Chem. Soc. Rev. 48, 1712–1740 (2019).
2. Ko, S. H. et al. All-inkjet-printed flexible electronics fabrication on a polymer substrate by low-temperature high-resolution selective laser sintering of metal nanoparticles. Nanotechnology 18 https://doi.org/10.1088/0957-4484/18/34/345202 (2007).
3. Lewis, J. A. & Ahn, B. Y. Three-dimensional printed electronics. Nature 518, 42–43 (2015).
4. Saleh, E. et al. 3D inkjet printing of electronics using UV conversion. Adv. Mater. Technol. 2, 2–9 (2017).
5. Vaithilingam, J. et al. Combined inkjet printing and infrared sintering of silver nanoparticles using a swathe-by-swathe and layer-by-layer approach for 3-dimensional structures. ACS Appl. Mater. Interfaces 9, 6560–6570 (2017).
6. Begines, B. et al. Design of highly stabilized nanocomposite inks based on biodegradable polymer-matrix and gold nanoparticles for inkjet printing. Sci. Rep. 9, 1–12 (2019).
7. Zhang, F. et al. Reactive material jetting of polyimide insulators for complex circuit board design. Addit. Manuf. 25, 477–484 (2019).
8. Fernandes, I. J. et al. Silver nanoparticle conductive inks: synthesis, characterization, and fabrication of inkjet-printed flexible electrodes. Sci. Rep. 10, 1–11 (2020).
9. Sasan, K. et al. Additive manufacturing of optical quality germania-silica glasses. ACS Appl. Mater. Interfaces 12, 6736–6741 (2020).
10. Shi, L. et al. In situ inkjet printing strategy for fabricating perovskite quantum dot patterns. Adv. Funct. Mater. 29, 1–6 (2019).
11. Chiolerio, A., Bocchini, S. & Porro, S. Inkjet printed negative supercapacitors: synthesis of polyaniline-based inks, doping agent effect, and advanced electronic devices applications. Adv. Funct. Mater. 24, 3375–3383 (2014).
12. Tiberto, P. et al. Magnetic properties of jet-printer inks containing dispersed magnetite nanoparticles. Eur. Phys. J. B 86, 2–7 (2013).
13. Jeon, H., Hong, S. K., Kim, M. S., Cho, S. J. & Lim, G. Omni-purpose stretchable strain sensor based on a highly dense nanocracking structure for whole-body motion monitoring. ACS Appl. Mater. Interfaces 9, 41712–41721 (2017).
14. Liu, S. et al. Laser sintering of liquid metal nanoparticles for scalable manufacturing of soft and flexible electronics. ACS Appl. Mater. Interfaces 10, 28232–28241 (2018).
15. Tavakoli, M. et al. EGaIn-assisted room-temperature sintering of silver nanoparticles for stretchable, inkjet-printed, thin-film electronics. Adv. Mater. 30, 1–7 (2018).
16. Chen, S. P., Kao, Z. K., Lin, J. L. & Liao, Y. C. Silver conductive features on flexible substrates from a thermally accelerated chain reaction at low sintering temperatures. ACS Appl. Mater. Interfaces 4, 7064–7068 (2012).
17. Zhai, Q. et al. Vertically aligned gold nanowires as stretchable and wearable epidermal ion-selective electrode for noninvasive multiplexed sweat analysis. Anal. Chem. https://doi.org/10.1021/acs.analchem.0c00274 (2020).
18. Carey, T. et al. Fully inkjet-printed two-dimensional material field-effect heterojunctions for wearable and textile electronics. Nat. Commun. 8 https://doi.org/10.1038/s41467-017-01210-2 (2017).
19. Zhang, S. et al. Fully printed silver-nanoparticle-based strain gauges with record high sensitivity. Adv. Electron. Mater. 3, 1–6 (2017).
20. Liu, Y. et al. Inkjet-printed unclonable quantum dot fluorescent anti-counterfeiting labels with artificial intelligence authentication. Nat. Commun. 10, 1–9 (2019).
21. Kim, B. H. et al. High-resolution patterns of quantum dots formed by electrohydrodynamic jet printing for light-emitting diodes. Nano Lett. 15, 969–973 (2015).
22. Hu, Z. et al. Inkjet printed uniform quantum dots as color conversion layers for full-color OLED displays. Nanoscale 12, 2103–2110 (2020).
23. Li, T. et al. Additive engineering for highly efficient organic-inorganic halide perovskite solar cells: recent advances and perspectives. J. Mater. Chem. A 5, 12602–12652 (2017).
24. Huckaba, A. J. et al. Inkjet-printed mesoporous TiO2 and perovskite layers for high efficiency perovskite solar cells. Energy Technol. 7, 317–324 (2019).
25. Mathies, F., List-Kratochvil, E. J. W. & Unger, E. L. Advances in inkjet-printed metal halide perovskite photovoltaic and optoelectronic devices. Energy Technol. 1900991. https://doi.org/10.1002/ente.201900991 (2019).
26. Mathies, F. et al. Multipass inkjet printed planar methylammonium lead iodide perovskite solar cells. J. Mater. Chem. A 4, 19207–19213 (2016).
27. Sowade, E. et al. Roll-to-roll infrared (IR) drying and sintering of an inkjet-printed silver nanoparticle ink within 1 second. J. Mater. Chem. C 3, 11815–11826 (2015).
28. Niittynen, J. et al. Alternative sintering methods compared to conventional thermal sintering for inkjet printed silver nanoparticle ink. Thin Solid Films 556, 452–459 (2014).
29. Magdassi, S., Grouchko, M., Berezin, O. & Kamyshny, A. Triggering the sintering of silver nanoparticles at room temperature. ACS Nano 4, 1943–1948 (2010).
30. Vaithilingam, J. et al. 3-dimensional inkjet printing of macro structures from silver nanoparticles. Mater. Des. 139, 81–88 (2018).
31. Balliu, E. et al. Selective laser sintering of inkjet-printed silver nanoparticle inks on paper substrates to achieve highly conductive patterns. Sci. Rep. 8, 2–10 (2018).
32. Su, R., Park, S. H., Li, Z. & McAlpine, M. C. 3D printed electronic materials and devices. Robot. Syst. Auton. Platforms 2019, 309–334. https://doi.org/10.1016/b978-0-08-102260-3.00013-5 (2019).
33. Mohapatra, P. et al. Calcination does not remove all carbon from colloidal nanocrystal assemblies. Nat. Commun. 8 https://doi.org/10.1038/s41467-017-02267-9 (2017).
34. Chiolerio, A. et al. Ag nanoparticle-based inkjet printed planar transmission lines for RF and microwave applications: considerations on ink composition,

nanoparticle size distribution and sintering time. *Microelectron. Eng.* **97**, 8–15 (2012).

35. Frosch, T., Chan, K. L. A., Wong, H. C., Cabral, J. T. & Kazarian, S. G. Nondestructive three-dimensional analysis of layered polymer structures with chemical imaging. *Langmuir* **26**, 19027–19032 (2010).

36. Bailey, J. et al. 3D ToF-SIMS imaging of polymer multilayer films using argon cluster sputter depth profiling. *ACS Appl. Mater. Interfaces* **7**, 2654–2659 (2015).

37. Taylor, M. et al. Cluster sputter depth profiling 3D chemical characterization of frozen hydrated hydrogels using ToF-SIMS with argon cluster sputter depth profiling. *Biointerphases* **301**, https://doi.org/10.1116/1.4928209 (2016).

38. Singh, A. V. et al. ToF-SIMS 3D imaging unveils important insights on the cellular microenvironment during biomineralization of gold nanostructures. *Sci. Rep.* **10**, 1–11 (2020).

39. Cristaudo, V., Collette, S., Poleunis, C., Reniers, F. & Delcorte, A. Surface analysis and ultra-shallow molecular depth-profiling of polyethylene treated by an atmospheric Ar-D$_2$O post-discharge. *Plasma Process. Polym.* **12**, 919–925 (2015).

40. Cristaudo, V. et al. Molecular surface analysis and depth-profiling of polyethylene modified by an atmospheric Ar-D2O post-discharge. *Plasma Process. Polym.* **13**, 1104–1117 (2016).

41. Mouhib, T. et al. Molecular depth profiling of organic photovoltaic heterojunction layers by ToF-SIMS: comparative evaluation of three sputtering beams. *Analyst* **138**, 6801–6810 (2013).

42. Liu, Y., Lorenz, M., Ievlev, A. V. & Ovchinnikova, O. S. Secondary ion mass spectrometry (SIMS) for chemical characterization of metal halide perovskites. *Adv. Funct. Mater.* **2002**, 2002201 (2020).

43. Luo, D. et al. Enhanced photovoltage for inverted planar heterojunction perovskite solar cells. *Science* **360**, 1442–1446 (2018).

44. Tiddia, M. et al. Chemical imaging of buried interfaces in organic-inorganic devices using focused ion beam-time-of-flight-secondary-ion mass spectrometry. *ACS Appl. Mater. Interfaces* **11**, 4500–4506 (2019).

45. Iida, S., Carr, D. M., Fisher, G. L. & Miyayama, T. Accurate and reproducible in-depth observation of organic–inorganic hybrid materials using FIB-TOF-SIMS. *J. Vac. Sci. Technol. B* **36**, 03F107 (2018).

46. Yang, L. et al. Depth profiling and melting of nanoparticles in secondary ion mass spectrometry (SIMS). *J. Phys. Chem. C* **117**, 16042–16052 (2013).

47. Priebe, A. et al. 3D imaging of nanoparticles in an inorganic matrix using TOF-SIMS validated with STEM and EDX. *Anal. Chem.* **91**, 11834–11839 (2019).

48. Nanoparticles, S. & Shard, A. G. A straightforward method for interpreting XPS data from core-shell nanoparticles. *J. Phys. Chem. C* https://doi.org/10.1021/jp305267d (2012).

49. Konarski, P., Iwanejko, I. & Mierzejewska, A. SIMS Depth pro® Ling of Working Environment Nanoparticles. **2003**, 204, 757–761.

50. Tune, I., Suzer, S., Correa-Duarte, M. A. & Liz-Marzán, L. M. XPS characterization of Au (Core)/SiO2 (shell) nanoparticles. *J. Phys. Chem. B* **109**, 7597–7600 (2005).

51. Baer, D. R., Gaspar, D. J., Nachimuthu, P., Techane, S. D. & Castner, D. G. Application of surface chemical analysis tools for characterization of nanoparticles. *Anal. Bioanal. Chem.* **396**, 983–1002 (2010).

52. Baer, D. R. et al. Surface characterization of nanomaterials and nanoparticles: important needs and challenging opportunities. *J. Vac. Sci. Technol. A* **31**, 050820 (2013).

53. Smith, E. F. et al. Sample rotation improves gas cluster sputter depth profiling of polymers. *Surf. Interface Anal.* **49**, 953–959 (2017).

54. Passarelli, M. K. et al. The 3D OrbiSIMS—label-free metabolic imaging with subcellular lateral resolution and high mass-resolving power. *Nat. Methods* https://doi.org/10.1038/nmeth.4504 (2017).

55. Kang, S. W. & Kang, Y. S. Silver nanoparticles stabilized by crosslinked poly (vinyl pyrrolidone) and its application for facilitated olefin transport. *J. Colloid Interface Sci.* **353**, 83–86 (2011).

56. Koczkur, K. M., Mourdikoudis, S., Polavarapu, L. & Skrabalak, S. E. Polyvinylpyrrolidone (PVP) in nanoparticle synthesis. *Dalt. Trans.* **44**, 17883–17905 (2015).

57. Deegan, R. D. et al. Capillary flow as the cause of ring stains from dried liquid drops. *Nature* **389**, 827–829 (1997).

58. Deegan, R. D. et al. Contact line deposits in an evaporating drop. *Phys. Rev. E Stat. Phys. Plasmas Fluids Relat. Interdiscip. Top.* **62**, 756–765 (2000).

59. Hu, H. & Larson, R. G. Marangoni effect reverses coffee-ring depositions. *J. Phys. Chem. B* **110**, 7090–7094 (2006).

60. Wang, F. et al. Inter-flake quantum transport of electrons and holes in inkjet-printed graphene devices. *Adv. Funct. Mater.* https://doi.org/10.1002/adfm.202007478 (2020).

61. Harvey, S. P. et al. Understanding measurement artifacts causing inherent cation gradients in depth profiles of perovskite photovoltaics with TOF-SIMS. *Conf. Rec. IEEE Photovolt. Spec. Conf.* 1487–1490. https://doi.org/10.1109/PVSC40753.2019.8980549 (2019).

62. Harvey, S. P., Messinger, J., Zhu, K., Luther, J. M. & Berry, J. J. Investigating the effects of chemical gradients on performance and reliability within perovskite solar cells with TOF-SIMS. *Adv. Energy Mater.* **10**, 1–12 (2020).

63. Xian, J., Hua, Q., Jiang, Z., Ma, Y. & Huang, W. Size-dependent interaction of the poly(N-vinyl-2-pyrrolidone) capping ligand with Pd nanocrystals. *Langmuir* **28**, 6736–6741 (2012).

64. Mdluli, P. S. et al. Selective adsorption of PVP on the surface of silver nanoparticles: a molecular dynamics study. *J. Mol. Struct.* **1004**, 131–137 (2011).

65. Kyrychenko, A., Korsun, O. M., Gubin, I. I., Kovalenko, S. M. & Kalugin, O. N. Atomistic simulations of coating of silver nanoparticles with poly (vinylpyrrolidone) oligomers: effect of oligomer chain length. *J. Phys. Chem. C* **119**, 7888–7899 (2015).

66. Rossi, L. M., Fiorio, J. L., Garcia, M. A. S. & Ferraz, C. P. The role and fate of capping ligands in colloidally prepared metal nanoparticle catalysts. *Dalt. Trans.* **47**, 5889–5915 (2018).

67. Safo, I. A., Werheid, M., Dosche, C. & Oezaslan, M. The role of polyvinylpyrrolidone (PVP) as a capping and structure-directing agent in the formation of Pt nanocubes. *Nanoscale Adv.* **1**, 3095–3106 (2019).

68. Knopp, M. M. et al. Influence of polymer molecular weight on drug-polymer solubility: a comparison between experimentally determined solubility in PVP and prediction derived from solubility in monomer. *J. Pharm. Sci.* **104**, 2905–2912 (2015).

69. Alahmad, A., Eleoui, M., Falah, A. & Alghoraibi, I. Preparation of colloidal structural characterization. *Phys. Sci. Res. Int.* **1**, 89–96 (2013).

70. Black, K. et al. Silver ink formulations for sinter-free printing of conductive films. *Sci. Rep.* **6**, 1–7 (2016).

71. Trindade, G. F., Abel, M. & Watts, J. F. SimsMVA: a tool for multivariate analysis of ToF-SIMS datasets. *Chemom. Intell. Lab. Syst.* https://doi.org/10.1016/j.chemolab.2018.10.001 (2018).

72. Keenan, M. R. & Smentkowski, V. S. The statistics of ToF-SIMS data revisited and introduction of the empirical Poisson correction. *Surf. Interface Anal.* **48**, 218–225 (2016).

Acknowledgements

Author contributions
G.F.T., F.W., Y.H., C.J.T., R.H. and C.J.R. conceived and planned the experiments. G.F.T. carried out the chemical characterisation, data analysis and interpretation supported by Y.H., J.I., D.S., I.G., M.T., L.T., R.W., R.H. and C.J.R. G.F.T., A.B. and D.P. carried out electron microscopy. F.W., Y.H. and A.B. produced all AgNPs samples. D.P. carried out the thermogravimetry analysis. E.S. designed and produced the encapsulated conductive pattern supported by C.J.T. F.W. carried out the resistivity tests supported by J.I., L.T. and C.J.T. All authors provided critical feedback and wrote the manuscript.

Competing interests
The authors declare no competing interests.

Additional information